

Magnetic Excitations in CoO

Keisuke TOMIYASU* and Shinichi ITOH

*Neutron Science Laboratory, Institute of Material and Structure Science,
 High Energy Accelerator Research Organization, 1-1 Oho, Tsukuba, Ibaraki 305-0801*

(Received November 25, 2005; accepted June 14, 2006; published August 10, 2006)

Magnetic excitations in CoO below $T_N = 289$ K were investigated on single crystals and a powder specimen by using inelastic neutron-scattering spectrometers installed at a steady state neutron-source and a pulsed neutron source. In single-crystal data, dispersion relations of the two magnetic excitation modes below 70 meV were determined along the symmetric directions. The magnetic excitations around 120 meV were also observed. Energy spectra on a powder specimen suggest the existence of higher order magnetic excitations spreading up to around 200 meV. The magnetic modes were analyzed in connection with the freedom of an unquenched orbital angular-momentum L of a Co^{2+} ion. The magnitude of the spin-orbit interaction and that of the exchange interaction obtained from the analyses are comparable, indicating that those interactions must be simultaneously considered without an approximation of the total-angular-momentum. The lowest two dispersion curves are interpreted as mixing and splitting between a dispersive excitation of S_z (S -mode) and an individual excitation of L_z (L -mode). The present experiments are the first observation of such hybridization of the S -mode and the L -mode.

KEYWORDS: neutron-scattering, orbital angular-momentum, spin-orbit interaction, magnon-phonon coupling, orbital wave, quadrupole wave

DOI: [10.1143/JPSJ.75.084708](https://doi.org/10.1143/JPSJ.75.084708)

1. Introduction

An orbital angular-momentum L , not only a spin angular-momentum S , generates a magnetic moment. Therefore, magnetic excitations in systems with L should provide the most fundamental knowledge about magnetism. One treats the Hamiltonian $H_{\text{ex}} = \sum_{i,j} J_{ij} \mathbf{S}_i \mathbf{S}_j$ without L , when L is quenched. If L is unquenched, like in f -electron magnets, the total-angular-momentum, $\mathbf{J} = \mathbf{L} + \mathbf{S}$, namely J and J_z , are regarded as good quantum numbers owing to a large spin-orbit interaction. However, d -electron clouds spatially spread compared to f -electron clouds, and the spin-orbit coupling-constant λ is roughly proportional to $1/r^3$, where r is the distance between an electron and an atomic nuclear. Therefore, it is possible that the approximation of \mathbf{J} is not applied for d -electron magnets with unquenched L , in which the magnitude of the spin-orbit interaction can be close to that of the exchange interaction. In such systems, we must directly consider the Hamiltonian $H_{\text{so}} + H_{\text{ex}} = \sum_i \lambda_i L_i S_i + \sum_{i,j} J_{ij} \mathbf{S}_i \mathbf{S}_j$; therefore, it is prospective that the effect of L explicitly appears.^{1,2)}

Approaches to remove the approximation of \mathbf{J} were tried early only on three collinear antiferromagnets of CoO (NaCl-type crystal-structure, $T_N = 289$ K), KCoF_3 (Perovskite-type crystal-structure, $T_N = 114$ K) and CoF_2 (Rutile-type crystal-structure, $T_N = 38$ K) by inelastic neutron-scattering,³⁻⁷⁾ as far as we know. Although one up moment is included in a magnetic unit-cell in these Co compounds, two or more magnetic modes were observed owing to the freedom of unquenched L of a Co^{2+} ion. The quantities J and J_z were approximately understood as good quantum numbers in the modes.⁵⁾

Since CoO exhibits the largest value of T_N , suggesting a strong superexchange interaction among the materials, the magnitude of the exchange interaction can become closest to

that of the spin-orbit interaction. In addition, magnetic excitations in CoO were measured with dispersion relations of phonons around the Γ point of a lattice in earlier studies.³⁾ Therefore, it will be worth determining the dispersion relations of magnetic excitations in CoO around a magnetic Γ point, in order to study the effect of L .

Figures 1(a) and 1(b) show the trajectories of the electronic states of a single Co^{2+} ion for $H_{\text{so}} \gg H_{\text{ex}}$ and $H_{\text{so}} \approx H_{\text{ex}}$, respectively. Following Hund's rule, the $(3d)^7$ configuration of a free Co^{2+} ion is represented by 4F with $S = 3/2$ and $L = 3$. Five electrons keep a closed shell with an up-spin in the following explanation. In an octahedral crystal-field of O^{2-} ions, the 4F states come across with the Γ_4 orbital triplet-states as ground states of two remaining electrons with a down-spin. The Γ_4 states are described by $L = -(3/2)l$, where l is the effective orbital angular-momentum with $l = 1$.¹⁾ Note that the classification of $d\gamma$ doublet-states and $d\epsilon$ triplet-states, which are convenient for describing an one electron, are not good quantum states of each electron.⁸⁾ Complicated combinations of two-electron states based on the $d\gamma$ and $d\epsilon$ states give the Γ_4 states.¹⁾ In Fig. 1(a), the spin-orbit interaction resolves the Γ_4 states into states with $J = 1/2, 3/2$ and $5/2$, where $\mathbf{J} = \mathbf{l} + \mathbf{S}$. Since the real total-angular-momentum $\mathbf{L} + \mathbf{S}$ does not appear in all of the following sections, we use the letter \mathbf{J} for the effective total angular momentum. Then, the $J = 1/2, 3/2$ and $5/2$ states are completely split into non-degenerated-states with $J_z = \pm 1/2, J_z = \pm 1/2, \pm 3/2$ and $J_z = \pm 1/2, \pm 3/2, \pm 5/2$, respectively, by the mean field of the Heisenberg exchange interaction.^{3,5)} When the states with different J do not cross each other, as shown in Fig. 1(a), J and J_z can be approximately understood as good quantum numbers. In Fig. 1(b), the spin-orbit interaction and the mean field of the Heisenberg exchange interaction must be simultaneously brought in the Γ_4 states, and only J_z survives as a good quantum number (see Appendix for further mathematical subjects). Finally, in both (a) and (b), the rest

*E-mail: keisuke.tomiyasu@kek.jp

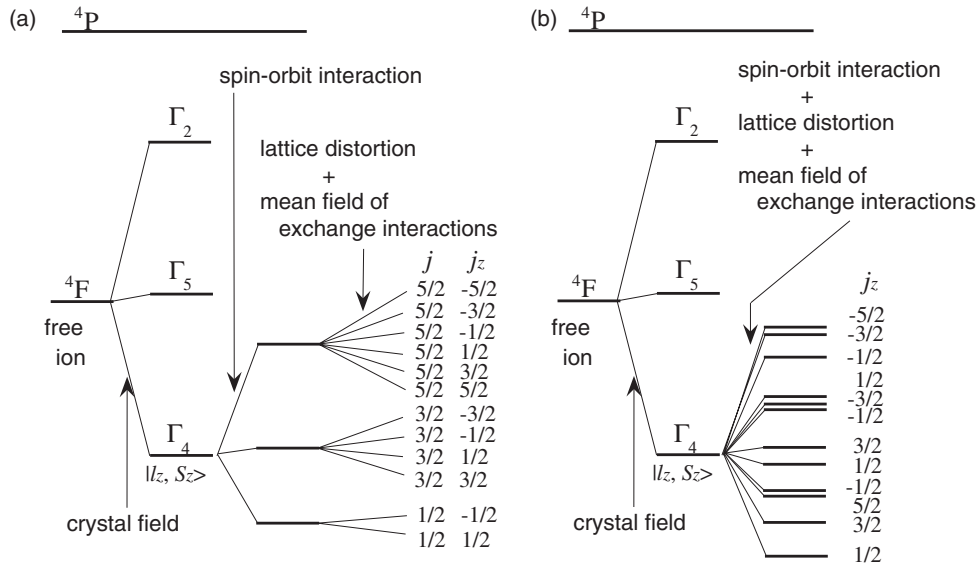


Fig. 1. Energy-level schemes of a single-ion state of a Co^{2+} ion for $H_{\text{so}} \gg H_{\text{ex}}$ (a) and $H_{\text{so}} \approx H_{\text{ex}}$ (b). The twelve-fold Γ_4 states (orbital-triplet \times spin-quadruplet) are represented by an effective orbital angular-momentum, $l = 1$, and a spin angular-momentum, $S = 3/2$. The degree of splitting and the longitudinal levels of the twelve lines in the most right side in (a) and (b) depend on the magnitude of the spin-orbit interaction, the anisotropy energy and the exchange interaction.

of the Heisenberg exchange interaction diagonalizes the magnetic excitons from the single-ion ground state to all of the single-ion excited states, and propagates them with some propagation vector (a magnetic exciton model).⁵⁾ We expect that magnetic excitations in CoO are represented by propagation of the J_z -states as shown in Fig. 1(b).

In this present paper, we consider magnetic excitations in CoO below T_N by inelastic neutron-scattering on single-crystal specimens and a powder specimen. In §2, experiments on a steady state neutron-source and a pulsed neutron source are described. In §3, the Q -dependence and temperature dependence of the energy spectra at and around a magnetic Γ point are shown. Dispersion relations of magnetic excitations at 150 K are also given. In §4, the dispersion curves are calculated in the magnetic exciton model. Results of the analyses and pictures of the magnetic modes are discussed. The conclusions are summarized in §5. Mathematical subjects used for the analyses are explained in Appendix.

2. Experiments

Single-crystal neutron-scattering experiments, A, were performed on the triple axis spectrometer PONTA installed at the JRR-3M reactor, Japan Atomic Energy Agency (JAEA), Tokai, Japan. The energy of the final neutrons was fixed at 30.5 meV. The energy range up to 50 meV was measured. The highest energy transfer (E) was limited to 50 meV by the geometric condition of the spectrometer. A pyrolytic graphite filter efficiently eliminated the higher order contamination. The horizontal collimator sequence was set to open-40'-40'-80'. The $(h h k)$ zone was taken as the scattering plane. A single-crystal specimen of CoO with a size of about $15 \times 8 \times 2 \text{ mm}^3$, which is the same specimen measured in the recent elastic neutron-scattering experiments,¹³⁾ was used. The specimen was enclosed with He exchange gas in an aluminum container, which was set under the cold head of a closed-cycle He refrigerator.

Single-crystal neutron-scattering experiments, B, were performed on the direct geometry chopper spectrometer INC installed at the pulsed spallation neutron-source, KENS, High Energy Accelerator Research Organization (KEK), Tsukuba, Japan.⁹⁾ The $(h h k)$ zone was also taken as the scattering plane. The energy of the incident neutrons (E_i) was fixed at 101, 201, and 509 meV when the incident beam was parallel to the $[001]$ direction, and was fixed at 152 and 506 meV when the incident beam was parallel to the $[110]$ direction. In the former setting, the vertical scattering-plane of the $(h h k)$ zone was equivalent to the horizontal scattering plane of the $(h h k)$ zone. On INC, the detector banks at low angles are mounted with the four-fold symmetry around the direct beam. The spectra at the detectors in the left-, right-, top-, and bottom-banks with the same scattering angle were summed in order to obtain higher statistics. In the latter setting, the spectra in the left- and right-detectors were summed. A single-crystal specimen of CoO with a size of about $5 \times 5 \times 5 \text{ mm}^3$ was used. The specimen was fixed under the head of an aluminum stick (3 mm ϕ) without an aluminum container in order to minimize the background. The aluminum stick was mounted under the cold head of a closed-cycle He refrigerator.

Powder neutron-scattering experiments, C, were also performed on INC. A powder specimen of CoO (Rare Metallic Corp., Japan) with a mass of 50 g and a purity of 99.9% was used. The sample was shaped with an area of $50 \times 50 \text{ mm}^2$, and was enclosed with He exchange gas in an aluminum container, which was secured to the cold head of a closed-cycle He refrigerator. The plate-sample was set to be perpendicular to the incident beam. The energy of the incident neutrons was fixed at 201 and 504 meV.

3. Results

3.1 Data at 150 K

We focused on measurements at 150 K to obtain representative data well below T_N , because the energy spectra at a

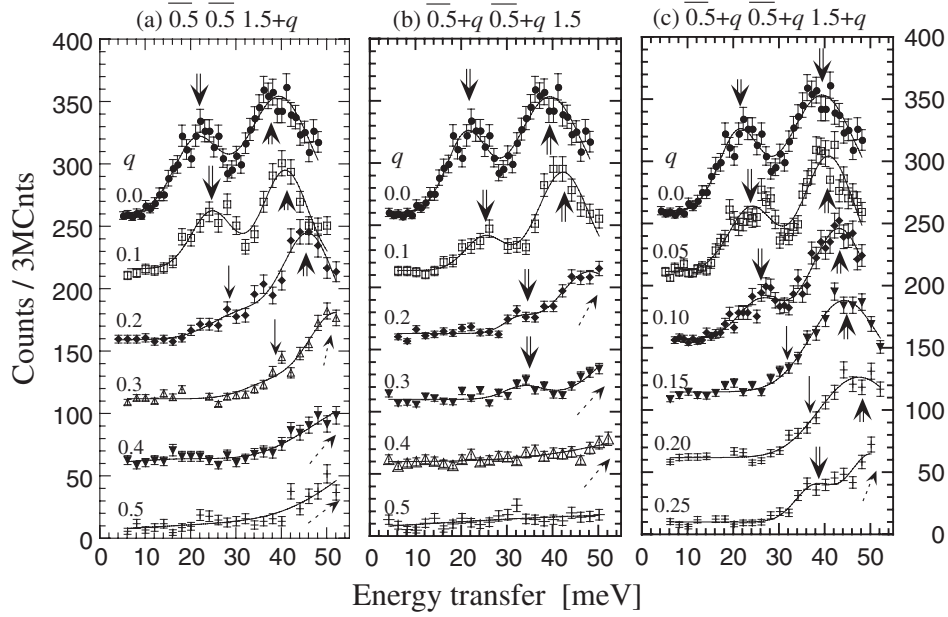


Fig. 2. Energy spectra measured at the $\overline{0.5} \overline{0.5} \overline{1.5} + q$ (a), $\overline{0.5} + q \overline{0.5} + q \overline{1.5}$ (b) and $\overline{0.5} + q \overline{0.5} + q \overline{1.5} + q$ (c) reciprocal lattice points at 150 K on PONTA by using a single-crystal specimen. The zero points of the vertical axis of the top four spectra are shifted to 250, 200, 150, 100, and 50 counts in the graphs (a), (b), and (c). Double-solid-line arrows and single-solid-line arrows indicate appreciable peak-tops and broad magnetic-scattering, respectively. Broken-single-line arrows mean magnetic scattering, whose peak-tops cannot be determined beyond the energy range of the present data. All of the lines are drawn by single-Gaussian or double-Gaussian fitting.

magnetic Γ point exhibit the strongest intensity at 150 K owing to thermal excitations, as shown in Fig. 8. The temperature dependence is mentioned in §3.2 for convenience of explanation.

Dispersion relations were determined by measuring the energy spectra at several Q points around a magnetic Γ point on single-crystal specimens. As the typical single-crystal data on PONTA, Figs. 2(a)–2(c) show the energy spectra measured around the $\overline{0.5} \overline{0.5} \overline{1.5}$ magnetic Γ point by the constant- Q mode along the [001], [110] and [111] directions at 150 K, respectively. The energy spectra at $q = 0.0$ shown in these three figures are identical. As the value of q increases, the two magnetic peaks shift towards the high energy side, meaning dispersive excitation modes. The first peaks in the spectra become broad and weak around 35 to 40 meV while receding from the magnetic Γ point, as shown by the single-solid arrows. No appreciable existence of the first peak can be read at $q = 0.4$ and 0.5 along the [001] and [110] directions. The energy of the second branch will be close to or be higher than 50 meV in the region of larger q , as shown by broken-single-line arrows.

The higher energy magnetic excitations were measured in single-crystal experiments on INC. The inelastic spectra were measured with $k_i \parallel$ [001] and [110] at $T = 150$ K, where k_i is the incident neutron wave vector. Figure 3(a) shows the energy spectra integrated in the range of $5.00 < 2\theta < 9.17^\circ$, $8.58 < 2\theta < 9.17^\circ$, and $6.19 < 2\theta < 7.98^\circ$ measured at $E_i = 101$, 152, and 201 meV, respectively, as the typical data of $E_i \lesssim 200$ meV. Figure 4(a) shows the energy spectra integrated in the range of $5.00 < 2\theta < 9.17^\circ$ measured at $E_i = 506$ meV and $k_i \parallel$ [110], as a part of the data of $E_i \simeq 500$ meV. Figures 3(b) and 4(b) show the corresponding scan-loci in the four-dimensional (Q, E) space projected on the scattering plane. The spectra of several detectors are merged within sharp sectors, shown in

Figs. 3(b) and 4(b), for higher statistics. The peak intensities are obtained at intersections or close points between dispersion curves and the scan-loci, and their positions in the (Q, E) space are roughly represented by ellipsoids in Figs. 3(b) and 4(b). In addition to the magnetic excitations below 50 meV, magnetic excitations in 50 to 60 meV and broad inelastic-magnetic-scattering around 120 meV are observed.

Figure 5 shows dispersion relations along the symmetric directions, obtained by plotting the solid or open marks at the positions of the peak-tops on the energy spectra in the above single-crystal data. The error-bars attached with the solid symbols are vertical along loci of constant- Q scans. Similarly, the diagonal error-bars are written along projections on the $(0, 0, q, E)$, $(q, q, 0, E)$, and (q, q, q, E) planes of scan-loci running in the four-dimensional (Q, E) space. The results in the single-crystal experiments on PONTA (solid marks) and INC (open marks) can lie on two smooth lines below 70 meV, as shown by the solid lines, which are explained in the next section (§4).

In order to confirm that the excitations are of magnetic origin, we measured the energy spectrum at the $\overline{2.5} \overline{2.5} \overline{2.5}$ reciprocal lattice point in addition to the $\overline{0.5} \overline{0.5} \overline{1.5}$ point on PONTA by using a single crystal. The $\overline{0.5} \overline{0.5} \overline{1.5}$ and $\overline{2.5} \overline{2.5} \overline{2.5}$ points are identified to be the Γ points of magnetic domains described by propagation vectors, $(0.5, 0.5, 0.5)$ and $(-0.5, -0.5, 0.5)$. Since the single crystal used for our experiments includes multi magnetic domains, the two magnetic reciprocal points can be regarded as equivalent. Figure 6 shows the two spectra. Two appreciable peaks are observed only at the low- Q point, indicating that the peaks are magnetic. The magnitude of the reciprocal lattice vectors is 2.5 and 6.4 \AA^{-1} , therefore, the latter intensity is estimated to be 3% of the former intensity by the Watson–Freeman’s form factor.¹⁰⁾ The disappearance of the

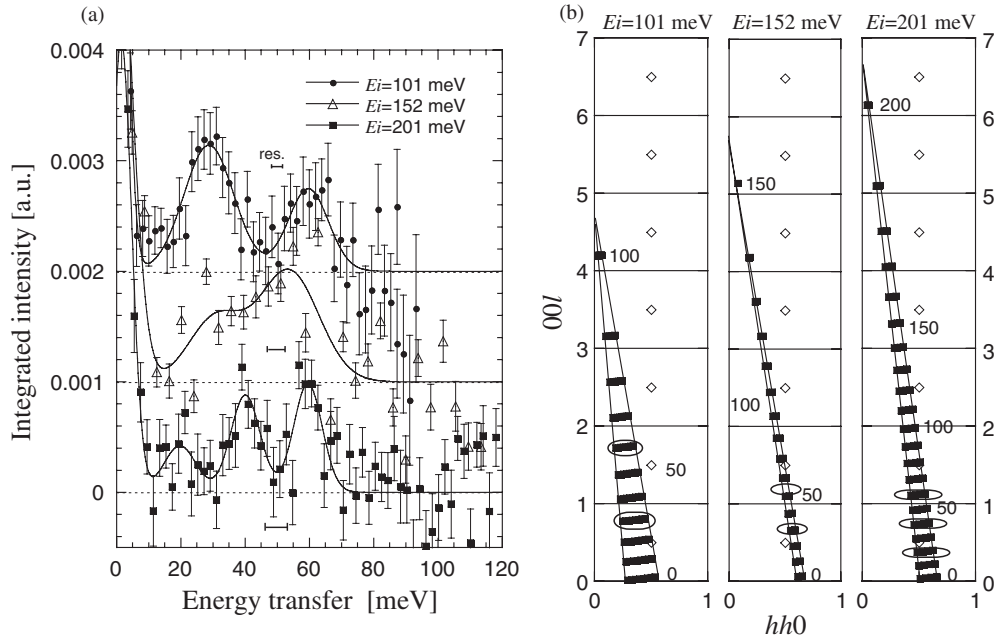


Fig. 3. (a) Energy spectra measured with $k_i \parallel [001]$ at $T = 150$ K on INC by using a single-crystal specimen. The intensities measured at $E_i = 101$, 152, and 201 meV were integrated in the range of $5.00 < 2\theta < 9.17^\circ$, $8.58 < 2\theta < 9.17^\circ$, and $6.19 < 2\theta < 7.98^\circ$, respectively. Zero points of the intensity are shown as broken horizontal lines. The solid lines are drawn by a triple-Gaussian or quadruple-Gaussian fitting including an elastic part. The energy resolutions around 50 meV are also shown in the figure. (b) Scan-areas projected on the scattering plane. The open squares indicate magnetic Γ points, and the numbers (0, 50, 100, 150, and 200) mean the values of energy transfer. The spectra in (a) are integrated within the sharp sectors in (b).

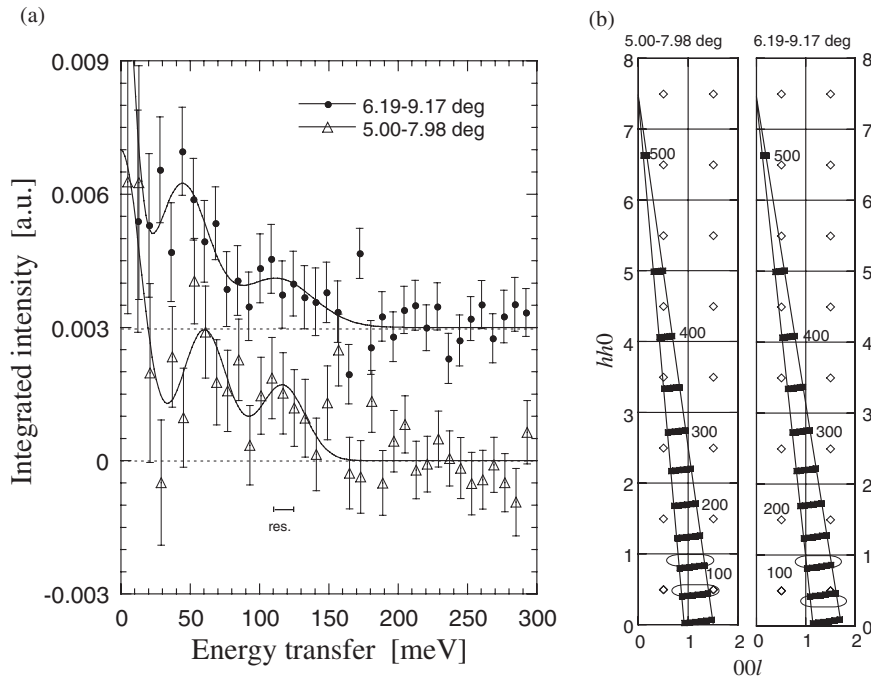


Fig. 4. (a) Energy spectra integrated in the range of $6.19 < 2\theta < 9.17^\circ$ and $5.00 < 2\theta < 7.98^\circ$ in the single-crystal data on INC. These data were measured at $E_i = 506$ meV, $k_i \parallel [110]$ and $T = 150$ K. The energy resolution around 120 meV is also shown in the figure. (b) Scan-areas projected on the scattering plane. In both (a) and (b), details are the same as those in Figs. 3(a) and 3(b).

latter peaks is also consistent with the results of powder data [Fig. 7(e)].

To further verify the energy range of magnetic scattering, we performed inelastic neutron-scattering experiments on a powder specimen of CoO at 150 K on INC. Figures 7(a) and 7(b) depict scan-loci of detectors at $E_i = 201$ and 504 meV. Figures 7(c) ($E_i = 201$ meV) and 7(d) ($E_i = 504$ meV) show

energy-spectra averaging over $5.00 < 2\theta < 11.56^\circ$ (low- Q) and $31.30 < 2\theta < 40.24^\circ$ (high- Q), of which scan-loci are described by shaded portions. A more precise Q -dependence of the intensity is shown in Figs. 7(e) ($E_i = 201$ meV) and 7(f) ($E_i = 504$ meV), where the intensity on each detector was integrated in every 20 or 50 meV to obtain higher statistics. By using the value of Q at the central energy in the

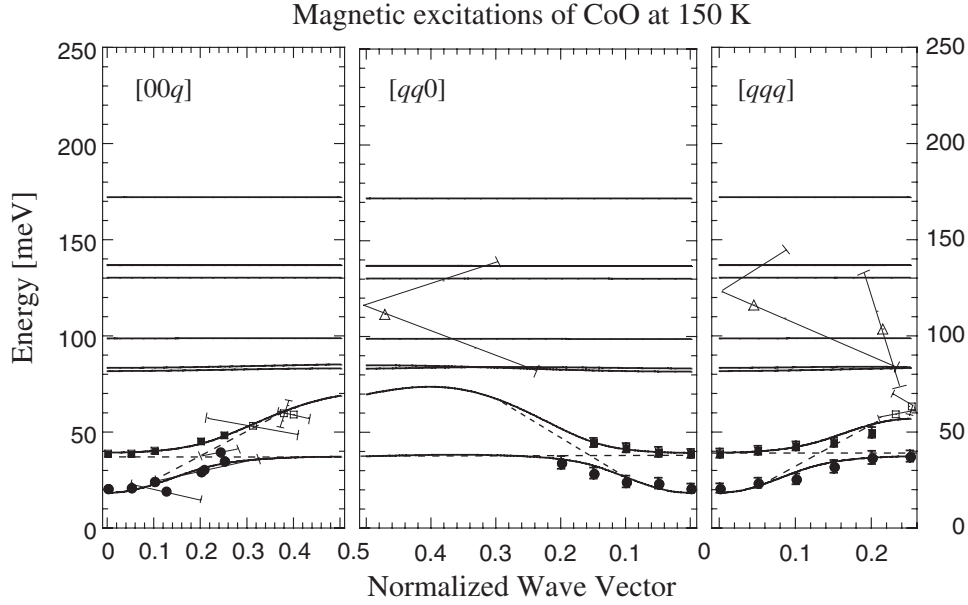


Fig. 5. Dispersion relations of magnetic excitations along the [001], [110], and [111] directions at 150 K in CoO. The solid circles and squares were obtained in single-crystal experiments on PONTA, and the open circles, squares and triangles were obtained in single-crystal experiments on INC. The solid lines show calculated dispersion-relations, obtained by fitting the positions of the plots with a magnetic-exciton model explained in the text body. The broken lines show the appearance before splitting of the two lowest modes.

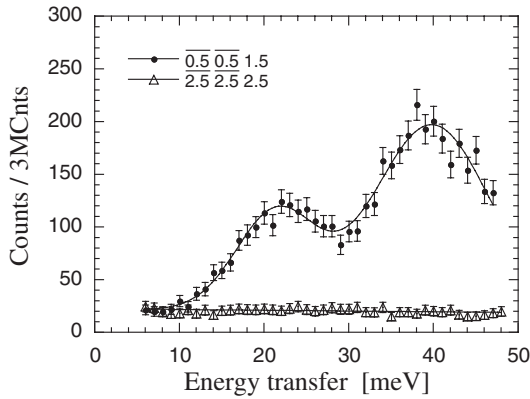


Fig. 6. Q -dependence of the energy spectra measured at the $\overline{0.5} \overline{0.5} \overline{1.5}$ and $\overline{2.5} \overline{2.5} \overline{2.5}$ reciprocal lattice points at 150 K on PONTA by using a single-crystal specimen. The upper line in (a) is drawn by double-Gaussian fitting.

integral interval, the Q -dependence corresponds to constant-energy scans, indicated by the double-solid-lines arrows in Figs. 7(a) and 7(b). Data of 200 to 250 meV in Fig. 7(f) are independent of Q . The other data exhibit the Q -dependence roughly described by the Watson–Freeman’s magnetic-form-factor,¹⁰⁾ which is shown by the lines in Figs. 7(e) and 7(f). Therefore, magnetic excitations exist at least up to 200 meV, including the energy range of 20 to around 120 meV observed in the single-crystal experiments on PONTA and INC.

3.2 Temperature dependence

Figure 8(a) shows the energy spectra measured on the $\overline{0.5} \overline{0.5} \overline{1.5}$ reciprocal lattice point (the magnetic Γ point) by the constant- Q mode at several temperatures below $T_N = 289$ K. The gap energy of the first mode decreases with increasing the temperature. Although the energy of the

second mode at the magnetic Γ point is constant within the statistical errors below T_N , the linewidth becomes broad with increasing the temperature. It is difficult to determine the peak-position above 230 K, meaning a short lifetime of the second mode. The temperature dependence of the values of the two peak-tops in Fig. 8(a) is summarized in Fig. 8(b).

Figures 9(a) and 9(b) show the energy spectra integrated from 5.00 to 11.56° , measured at $E_i = 201$ and 504 meV by using a powder specimen on INC, respectively. In Fig. 9(a), the peak around 60 meV at 10 K shifts towards the low-energy side and becomes weak with increasing the temperature. The magnetic scattering between 20 and 50 meV becomes soft and strong. In Fig. 9(b), temperature independency above around 100 meV is shown.

4. Discussion

We determined the dispersion relations of the two magnetic-excitation modes in the present experiments. In addition, higher order magnetic modes were found around 120 meV. All of the data are plotted in Fig. 5.

We fit the peak-positions of magnetic excitations below 70 meV observed in the present experiments by using the Hamiltonian

$$H = \lambda \sum_{\mu m} L_{\mu m} \cdot S_{\mu m} + c_{\parallel} \sum_{\mu m} L_{z\mu m}^2 + c_{\perp} \sum_{\mu m} (L_{x\mu m}^2 - L_{y\mu m}^2) + \sum_{\mu m} \sum_{\nu n} J_{\mu m \nu n} S_{\mu m} \cdot S_{\nu n}, \quad (1)$$

where c_{\parallel} and c_{\perp} are parameters of the anisotropy energy based on the analogy of the longitudinal and transverse spin anisotropy, respectively, z is the direction of the quantization axis of J_z , μ and ν are magnetic sublattices (up and down), m and n are magnetic unit-cells, $J_{\mu m \nu n}$ is the exchange integral between a magnetic moment at the μm site and another magnetic moment at the νn site. In the present analyses, to minimize the number of parameters, c_{\perp} was dropped and

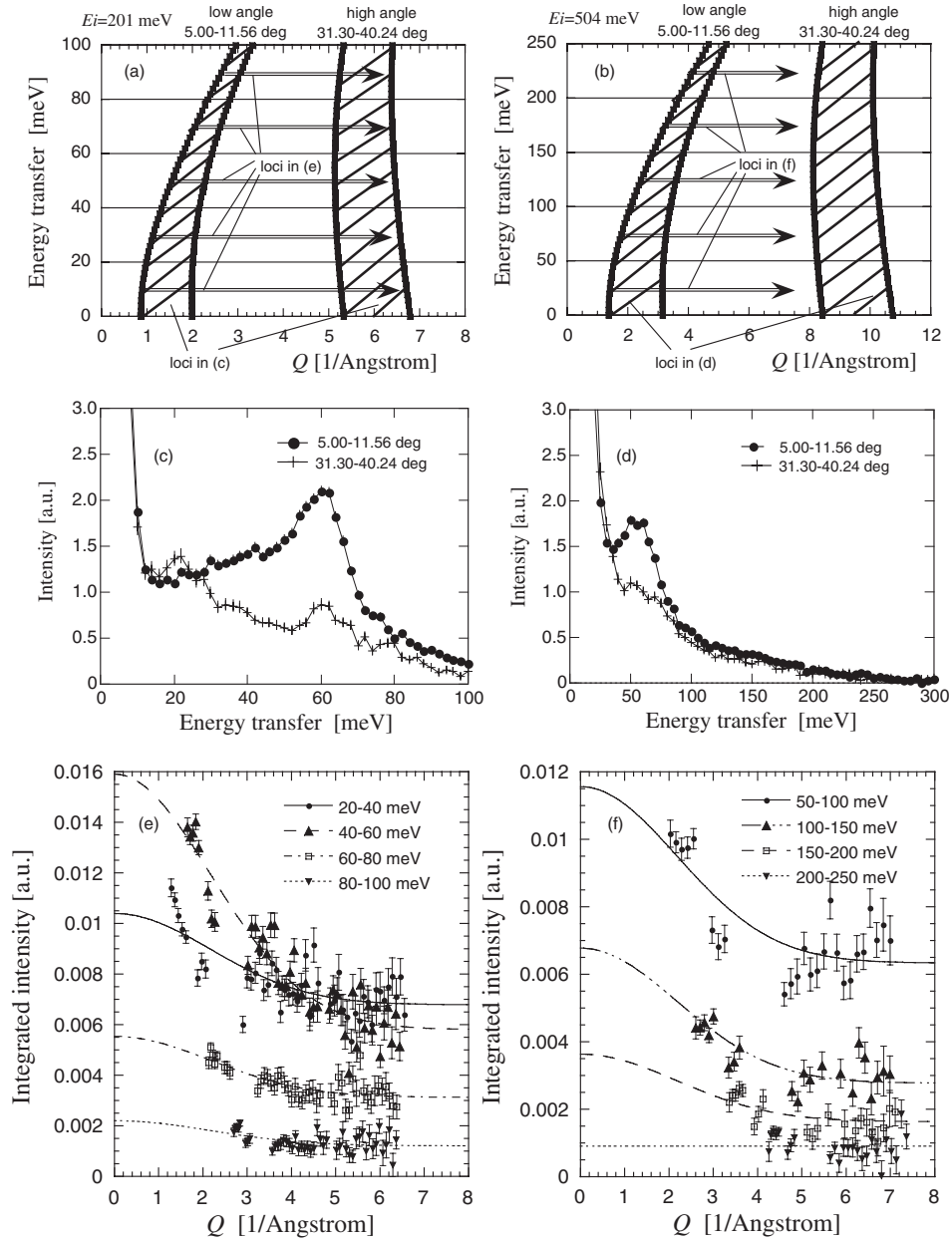


Fig. 7. (a, b) Scan-loci of detectors in the range of $5.00 < 2\theta < 11.56^\circ$ (low- Q) and $31.30 < 2\theta < 40.24^\circ$ (high- Q) at $E_i = 201$ and 504 meV in the (Q, E) space. (c, d) Energy spectra of the low- Q and high- Q , measured at $E_i = 201$ and 504 meV at 150 K on INC by using a powder specimen. (e, f) Q -dependence of the intensity integrated over the energy range of every 20 and 50 meV. Lines were drawn by fitting the data with the sum of the Watson-Freeman's magnetic form factor of a Co^{2+} ion¹⁰⁾ and a constant.

$J_{\mu\nu m}$ was restricted to the r th neighbor exchange interactions J_r . The constraint of J_r means that, for example, the nearest neighbor exchange integral between parallel magnetic moments J_{1p} and that between antiparallel ones J_{1ap} were not distinguished. Figure 10 shows the first, second and third neighbor exchange integrals, J_1 , J_2 , and J_3 . These treatments are the same treatments as those in the analyses of magnetic excitations in KCoF_3 .⁵⁾

The lattice in CoO is cubic above T_N , and becomes monoclinic below T_N because of the coexistence of tetragonal distortion and trigonal distortion ($|a - c|/a \simeq 1\%$ and $\Delta\beta \simeq 0.30^\circ$ at lowest temperatures).^{11,12)} The magnetic structure is also described by superposition of the trigonal type-II-structure with the propagation vector $(1/2, 1/2, 1/2)$ and the tetragonal type-I-structure with the propagation vector $(0, 0, 1)$.¹³⁾ In the following analyses, the effect of the

crystallographic and magnetic domains is ignored, because no appreciable splits of magnetic peaks coming from the domains were observed within the resolution in all of the present experiments. Also, since the magnitude of a component consisting of the type-I-structure in magnetic moments is less than 5% of that of the type-II-structure,¹³⁾ the magnetic structure of CoO is approximately regarded as a collinear type-II-structure.

The Hamiltonian, eq. (1), is solved by the magnetic exciton model developed by Buyers *et al.*⁵⁾ Although it is difficult to draw an intuitive picture of the magnetic exciton owing to the fact that only J_z is a good quantum number [Fig. 1(b)], the model is an extension of the linear spin wave theory (magnon) into systems with unquenched L . In the spin wave theory, by linearly combining the waves propagated in each sublattice,

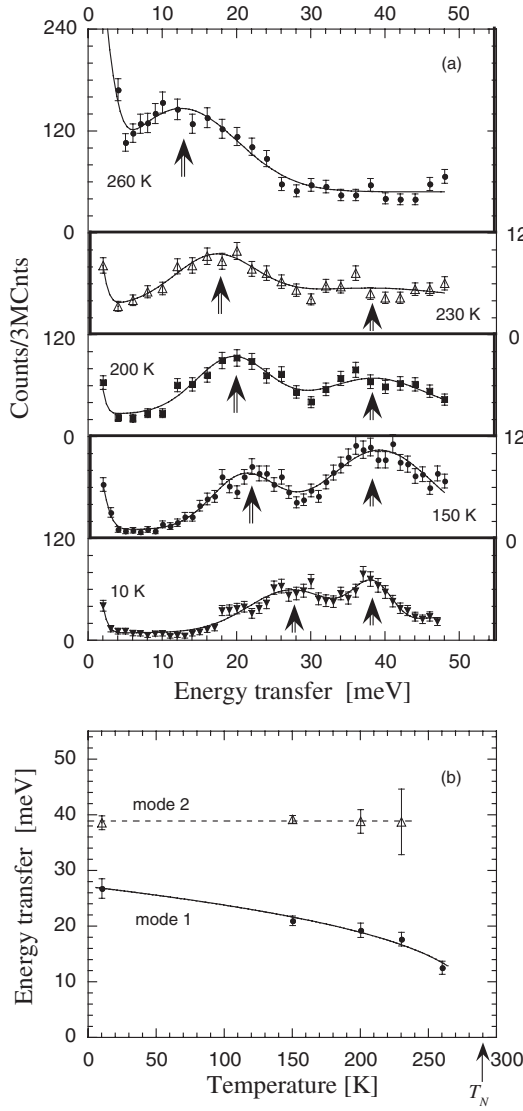


Fig. 8. (a) Temperature dependence of the energy spectra at the $0.5\ 0.5\ 1.5$ magnetic Γ point measured below $T_N = 289$ K in the single-crystal data on PONTA. Lines are drawn by double-Gaussian or triple-Gaussian fitting including an elastic part. (b) Temperature dependence of the energy at the magnetic Γ point of the first and second branches. The two lines are drawn for guide to the eyes.

$$|\Phi_\mu\rangle = \frac{1}{\sqrt{N_\mu}} \sum_m \exp(i\mathbf{q} \cdot \mathbf{r}_{\mu m}) \hat{a}_{\mu m}^\dagger |\Phi^{(0)}\rangle,$$

where N_μ is the number of magnetic ions in the sublattice μ , $\mathbf{r}_{\mu m}$ is the position vector of the μm site and $|\Phi^{(0)}\rangle$ is the ground state of the whole system, an antiferromagnetic magnon is formulated as

$$|\Phi\rangle = \sum_\mu c_\mu |\Phi_\mu(\mathbf{q})\rangle,$$

where c_μ is the coefficients given in the Bogoliubov transformation among the sublattices. The operator of $\hat{a}_{\mu m}^\dagger$ is represented by $\hat{S}_{-\mu m}/\sqrt{2S}$ or $\hat{S}_{+\mu m}/\sqrt{2S}$, and $S_{z\mu} = \sum_m S_{z\mu m}$ changes 1 compared to the ground state (magnon). Meanwhile, in systems with unquenched L , the operator of $\hat{a}_{\mu m}^\dagger$ is replaced by that of $\hat{a}_{\mu m}^\dagger(p)$ making a single-ion state at the μm site transit from $|0\rangle$ to $|p\rangle$ ($p = 1, \dots, 11$), where $|0\rangle$ is a single-ion ground state and $|p\rangle$ is a single-ion excited

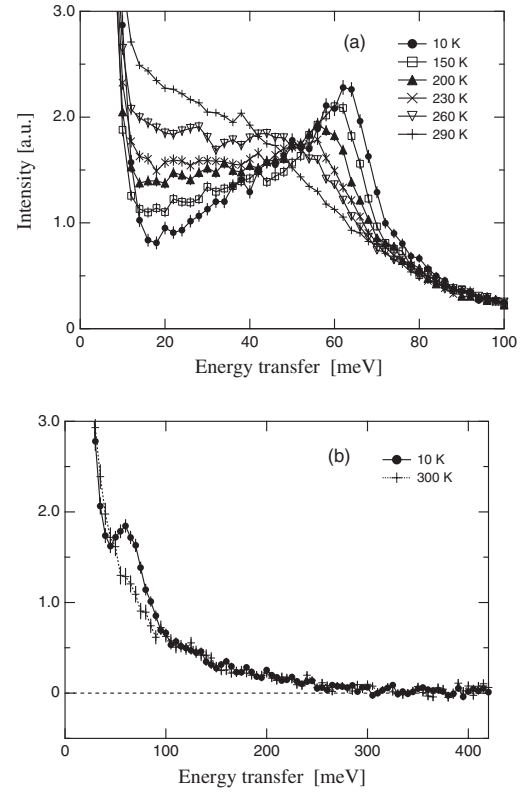


Fig. 9. Temperature dependence of the energy spectra integrated from 5.00 to 11.56° at $E_i = 201$ meV (a) and $E_i = 504$ meV (b) in the powder data on INC. All of the lines are polygonal for a guide to the eyes.

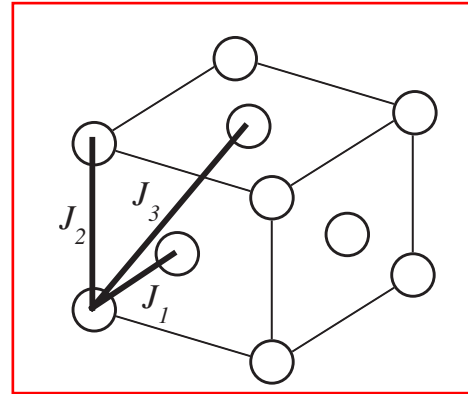


Fig. 10. First, second and third neighbor exchange integrals, J_1 , J_2 , and J_3 . The Co^{2+} ions form pseudo face-centered cubic unit cell in CoO.

state. The single-ion states in CoO are shown in Fig. 1(b). See Buyers *et al.*'s original paper for further mathematical subjects.⁵⁾

The solid lines in Fig. 5 show the calculated dispersion-curves, which best fit the peak-positions of the magnetic excitations below 70 meV obtained in the present experiments in a least-squares method. The calculated dispersion-curves pass through almost all of the points within the experimental errors. The results that the dispersive modes are located below about 80 meV in the calculation are also supported by the fact that the energy spectra on the powder specimen depend on the temperature only in the same energy region, because dispersivity suggests a collective excitation based on the antiferromagnetic order below T_N .

Table I. Parameters in the Hamiltonians among the related systems of KCoF₃, CoF₂, MnO, FeO, CoO, and NiO. The values of CoO are the results of the present fitting. $|h_{\text{ex}}|$ is the value of the mean field of the exchange interaction per a Co²⁺ ion, and $|h_{\text{so}}|$ is the value of the spin-orbit interaction per a Co²⁺ ion. The other quantities are defined in the text body. The symbol, “—”, means that the data of magnetic excitations were analyzed without the parameter.

	CoO	KCoF ₃	CoF ₂	MnO	FeO	NiO
T_N (K)	289	114	38	115	198	523
λ (meV)	−12	−17	−19	—	—	—
c_{\parallel} (meV)	−6.7	−0.49	−1.51	−0.03	−0.08	−0.052
c_{\perp} (meV)	—	—	—	−0.03	—	−0.048
J_1 (meV)	−0.31	1.30	−0.08	—	—	—
J_{1p} (meV)	—	—	—	0.43	−0.46	−1.39
J_{1ap} (meV)	—	—	—	0.32	−0.26	−1.35
J_2 (meV)	2.8	—	0.50	0.42	0.81	19.01
J_3 (meV)	−0.67	—	—	—	—	—
$ h_{\text{ex}} / h_{\text{so}} $	$\frac{38}{41} = 0.93$	$\frac{18}{59} = 0.31$	$\frac{6.8}{43} = 0.16$	—	—	—

The fitting parameters are given in Table I along with the parameters of KCoF₃, CoF₂, MnO, FeO, and NiO, also obtained from their dispersion curves of magnetic excitations determined by inelastic neutron-scattering.^{3–7,14–17)} The value of λ in CoO is less than 52% of $\lambda = 22$ meV for the free Co²⁺ ion,¹⁸⁾ indicating a spatial spreading of the 3d electron and the large superexchange interaction in CoO ($\lambda \propto 1/r^3$ roughly). The magnitude of c_{\parallel} in CoO is much larger than those of c_{\parallel} or c_{\perp} in the other compounds, reflecting that the crystallographic symmetry of CoO is the lowest below T_N . The lattice in CoO is monoclinic,¹²⁾ those in KCoF₃ and CoF₂ are tetragonal^{19,20)} and those in MnO, FeO, and NiO are trigonal.^{21–23)} The magnitude of $|J_1|$ and $|J_2|$ increases in accord with that of T_N among monoxides. The most dominant exchange integral is $|J_2|$ (180° superexchange interaction) in CoO as well as in the other monoxides.

The spin-orbit interaction per a Co²⁺ ion is calculated as $|h_{\text{so}}| = |\lambda L_z S_z| = (12 \cdot \frac{3}{2} \cdot \frac{3}{2}) = 41$ meV. On the other hand, a Co²⁺ ion is surrounded by six second-neighbor Co²⁺ ions with the same magnetic moment, and first and third neighbor Co²⁺ ions include the same numbers of up and down magnetic moments. Hence, the molecular field of the exchange interaction per a Co²⁺ ion is estimated to be $|h_{\text{ex}}| = |6 \cdot J_2 S_z S_z| = (6 \cdot 2.8 \cdot \frac{3}{2} \cdot \frac{3}{2}) = 38$ meV. Comparable values of 41 and 38 meV experimentally prove that the approximation of the total-angular-momentum cannot be used for CoO. For a comparison, Table I also gives the ratios of $|h_{\text{ex}}|$ to $|h_{\text{so}}|$ in KCoF₃ and CoF₂ obtained in a similar way.

The present fitting fails without J_3 . However, the necessity of J_3 should be recognized as a treatment for simplicity. The complex magnetic structure of CoO, in which the conventional type-II magnetic order is combined with the type-I magnetic order with a small magnitude of the magnetic moment (less than 5% of that of type-II), suggests the existence of magnetic geometric frustration and higher order kinematic exchange interactions, such as the biquadratic exchange interaction and the four body exchange interaction.¹³⁾ In addition to, or instead of, J_3 , the present data of magnetic excitations may be also reproduced by taking into account these complex interactions.

The Hamiltonian is separated into the a single-ion part H_1 and a term of an interaction between two ions H_2 (see

Appendix). The single-ion states identified in H_1 are summarized in Table II. All of the states are described by regarding only J_z as a good quantum number, not J and J_z . The ground state $|0\rangle$ consists dominantly of $|l_z, S_z\rangle = |-1, 3/2\rangle$, being consistent with the Kanamori theory.¹⁾ The magnitude of the magnetic moment for the ground state, $\langle \mu_z \rangle = \langle L_z \rangle + 2\langle S_z \rangle$, was obtained to be $4.29 \mu_B$, which is close to the value of $4.01 \mu_B$ for a theoretical ground state.²⁴⁾ The two lowest modes measured in the present experiments are identified to the crossing and splitting of a dispersive mode from $|0\rangle$ to $|3\rangle$ and a flat mode from $|0\rangle$ to $|1\rangle$, as represented by broken lines in Fig. 5. The state $|3\rangle$ is composed by a majority of $|-1, 1/2\rangle$, the transition from $|0\rangle$ to $|3\rangle$ is approximately equal to the decrease of 1 in S_z retaining the value of $l_z = -1$. Therefore, H_2 arising from the Heisenberg exchange interaction makes the magnetic exciton of $|3\rangle$ dispersive in the same mechanism as a usual spin-wave (S -mode). On the other hand, state $|1\rangle$ is mainly made of $|0, 3/2\rangle$, and the transition from $|0\rangle$ to $|1\rangle$ is approximately equivalent to the increase of 1 in l_z retaining the value of $S_z = 3/2$ (L -mode). Hence, the L -mode originally exhibits a flat dispersion. However, the S -mode and the L -mode mix and split around the crossing point of the broken lines in Fig. 5. Such splitting of the S -mode and the L -mode was observed in the present experiments for the first time, because the energy of the latter mode can be reduced to the energy region of the former mode, only when the spin-orbit interaction is comparable to the exchange interaction. It should be also noted that only transitions with $l_{z(\text{final})} - l_{z(\text{initial})} = 0, \pm 1$ or $S_{z(\text{final})} - S_{z(\text{initial})} = 0, \pm 1$, that is to say, $J_{z(\text{final})} - J_{z(\text{initial})} = 0, \pm 1$, are permitted in neutron-scattering. In Fig. 5, only dispersion curves with finite neutron-cross-section (solid lines) are shown.

Those interpretations are consistent with the temperature dependence of the energy spectrum at the magnetic Γ point shown in Fig. 8. The first peak is identified to be the gap energy of the S -mode. As the temperature increases towards T_N , the magnitude of the monoclinic lattice distortion continuously decreases towards cubic symmetry in CoO.^{11,12)} Since the anisotropy energy includes a corrective energy of crystal field through the lattice distortion, the shift of the first peak-positions can be interpreted as a decrease of the anisotropy energy. The

Table II. Information on single-ion states $|p\rangle$ identified in the present calculations. Energy is written in units of meV. The value of $\langle\mu_z\rangle = \langle L_z\rangle + 2\langle S_z\rangle = -\frac{3}{2}\langle l_z\rangle + 2\langle S_z\rangle$ is the magnitude of a magnetic moment in units of μ_B .

$ p\rangle$	Energy	J_z	$\langle l_z\rangle$	$\langle S_z\rangle$	$\langle\mu_z\rangle$	States on the base of $ l_z, S_z\rangle$
$ 0\rangle$	0	1/2	-0.94	1.44	4.29	$0.05 1, -1/2\rangle - 0.24 0, 1/2\rangle + 0.97 -1, -3/2\rangle$
$ 1\rangle$	38	3/2	0.15	1.35	0.07	$-0.39 1, 1/2\rangle + 0.92 0, 3/2\rangle$
$ 2\rangle$	59	5/2	1.00	1.50	-1.35	$1.00 1, 3/2\rangle$
$ 3\rangle$	63	-1/2	-0.89	0.39	2.10	$0.94 -1, 1/2\rangle - 0.32 0, -1/2\rangle + 0.08 1, -3/2\rangle$
$ 4\rangle$	84	1/2	0.27	0.23	-2.58	$-0.56 1, -1/2\rangle + 0.80 0, 1/2\rangle + 0.22 -1, 3/2\rangle$
$ 5\rangle$	99	3/2	0.85	0.65	-2.52	$0.92 1, 1/2\rangle + 0.39 0, 3/2\rangle$
$ 6\rangle$	130	-3/2	-0.89	-0.61	2.46	$0.94 0, -3/2\rangle - 0.33 -1, -1/2\rangle$
$ 7\rangle$	131	-1/2	0.43	-0.93	0.04	$-0.28 -1, 1/2\rangle - 0.64 0, -1/2\rangle + 0.71 1, -3/2\rangle$
$ 8\rangle$	137	1/2	0.67	-0.17	-2.61	$0.83 1, -1/2\rangle + 0.56 0, 1/2\rangle + 0.09 -1, 3/2\rangle$
$ 9\rangle$	172	-1/2	0.45	-0.95	0.11	$0.18 -1, 1/2\rangle + 0.70 0, -1/2\rangle + 0.69 1, -3/2\rangle$
$ 10\rangle$	200	-3/2	-0.11	-1.39	1.50	$0.33 0, -3/2\rangle + 0.94 -1, -1/2\rangle$
$ 11\rangle$	204	-5/2	-1.00	-1.50	-1.50	$1.00 -1, -3/2\rangle$

energy of the second peak is independent of the increase of the temperature, because the L -mode at the magnetic Γ point, which is away from the crossing point between the S -mode and the L -mode, can be regarded as an almost individual excitation of a Co^{2+} ion. The integrated intensities of individual excitations should survive even if the temperature increases towards T_N .

The spectra of the first modes are broad around 35 to 40 meV in Fig. 2. Since the mode is assigned as the L -mode, which is accompanied by a transformation of the shapes of electron clouds, it can be speculated that the energy of the L -mode escapes to phonons. The energy region of 35 to 40 meV matches the energy of the TO-phonon.³⁾ The TO-phonon leads to relative changes of the relative positions between Co^{2+} ions and O^{2-} ions; therefore, the L -mode can couple with TO-phonon through crystal field. Another possibility is a coupling of the L -mode with the magnetic excitation coming from the type-I antiferromagnetic order, which is too weak to observe in the present experiments because of the small magnitude of the type-I component in magnetic moments. The damping of the L -mode should be clarified in the future.

In the sense of a transformation in the shapes of electron clouds, the L -mode is common with an orbital wave and a quadrupole wave. However, the L -mode dominantly comes from the LS coupling energy. In addition, a Co^{2+} ion is characterized by a non-degenerate ground state, described by $J_z = 1/2$ shown in Fig. 1(b), CoO will exhibit ferro-orbital ordering. The L -mode should be distinguished from the orbital and quadrupole waves.

5. Conclusions

In the light of an unquenched orbital angular momentum in a Co^{2+} ion, we performed inelastic neutron-scattering experiments on single-crystal specimens and a powder specimen of CoO below $T_N = 289\text{ K}$. The dispersion curves of the two dispersive magnetic modes were determined around a magnetic Γ point along the $[001]$, $[110]$, and $[111]$ directions. Also, the higher order modes around 120 meV were found. The magnetic mode around 35 to 40 meV damps at the Q -region of the off-magnetic Γ point. The value of the energy of the first mode at the magnetic Γ point decreases and becomes soft with increasing the temperature towards T_N . That of the second mode is almost constant, but the

lifetime becomes shorter.

The magnetic-excitation modes are analyzed in connection with the freedom of the orbital angular-momentum. Furthermore, it was theoretically expected that the total-angular-momentum, $\mathbf{J} = \mathbf{L} + \mathbf{S}$, is not a good approximation in CoO, because d -electron clouds are spatially distributed compared to f -electron clouds, which can cause the small magnitude of the spin-orbit interaction near to the magnitude of the exchange interaction.¹⁾ In fact, the present analyses of the experimental data gave the comparable values of 41 and 38 meV for the spin-orbit interaction and the exchange interaction per a Co^{2+} ion, respectively. Therefore, it was experimentally proved that single-ion states of a Co^{2+} ion should be described by a single good quantum number, J_z , shown in Fig. 1(b).

The lowest two modes were interpreted as the mixing and splitting of the S -mode ($S_z \rightarrow S_z - 1$) and the L -mode ($l_z \rightarrow l_z + 1$). Only the competition between the spin-orbit interaction and the exchange interaction leads to such a splitting, which was observed in the present experiments for the first time. The temperature dependence of the first mode at the magnetic Γ point is consistent with the reduction of the monoclinic lattice-distortion¹²⁾ towards the cubic symmetry above T_N . The temperature dependence of the second mode at the magnetic Γ point is in agreement with the assignment of the mode as an individual excitation of the L -mode.

The damping of the L -mode at the region of off-zone-center is unresolved, and the higher energy region is still a new field. Experimentally and theoretically clarifying the overall picture of magnetic excitations in CoO will develop our understanding of fundamental magnetism as well as interactions accompanied by L , including magnon-phonon coupling.

Acknowledgment

We thank Professor H. Kondoh for supplying us the single crystals of CoO. We appreciate Professor Y. Tsunoda for his fruitful advice and discussion. We also thank Dr. M. Nishi and Dr. K. Nakajima for helping our experiments on PONTA. This work was partially supported by a Grant-in-Aid for Creative Scientific Research (No. 16GS0417) from the Ministry of Education, Culture, Sports, Science and Technology of Japan.

Appendix: Magnetic Exciton Model in CoO

The brief description of the magnetic exciton model,⁵⁾ used for the present analyses of magnetic excitations in CoO, is given. We provide a detailed explanation about only the formalization of the single-ion Hamiltonian, eqs. (A·4) and (A·5), to make Buyers *et al.*'s original paper more approachable. Characteristic parameters for CoO are summarized in the last paragraph.

For ease of use for the states $|l_z, S_z\rangle$, the Hamiltonian, eq. (1), is transformed into

$$H = \lambda' \sum_{\mu m} \mathbf{l}_{\mu m} \cdot \mathbf{S}_{\mu m} + c'_{\parallel} \sum_{\mu m} l_{z\mu m}^2 + \sum_{\mu m} \sum_{\nu n} J_{\mu m \nu n} \mathbf{S}_{\mu m} \cdot \mathbf{S}_{\nu n}, \quad (\text{A} \cdot 1)$$

where $c'_{\parallel} = \frac{9}{4} c_{\parallel}$ and $\lambda' = -\frac{3}{2} \lambda$. Next, the Hamiltonian is separated into the single-ion part H_1 and a term of an interaction between two ions at μm and νn sites,

$$H = H_1 + H_2$$

and

$$\begin{aligned} H_1\left(\pm \frac{1}{2}\right) &= \begin{pmatrix} -\frac{1}{2}\lambda' + c'_{\parallel} \mp \sum_r Z_r J_r \langle S_z^{(r)} \rangle & \sqrt{2}\lambda' & 0 \\ \sqrt{2}\lambda' & \pm \sum_r Z_r J_r \langle S_z^{(r)} \rangle & \frac{\sqrt{6}}{2}\lambda' \\ 0 & \frac{\sqrt{6}}{2}\lambda' & -\frac{3}{2}\lambda' + c'_{\parallel} \pm \sum_r Z_r J_r \langle S_z^{(r)} \rangle \end{pmatrix} \\ H_1\left(\pm \frac{3}{2}\right) &= \begin{pmatrix} \frac{1}{2}\lambda' + c'_{\parallel} \pm \sum_r Z_r J_r \langle S_z^{(r)} \rangle & \frac{\sqrt{6}}{2}\lambda' \\ \frac{\sqrt{6}}{2}\lambda' & \pm \sum_r Z_r J_r \langle S_z^{(r)} \rangle \end{pmatrix} \\ H_1\left(\pm \frac{5}{2}\right) &= \left(\frac{3}{2}\lambda' + c'_{\parallel} \pm \sum_r Z_r J_r \langle S_z^{(r)} \rangle\right), \end{aligned} \quad (\text{A} \cdot 4)$$

where $H_1(+\frac{1}{2})$, $H_1(-\frac{1}{2})$, $H_1(+\frac{3}{2})$, $H_1(-\frac{3}{2})$, $H_1(+\frac{5}{2})$ and $H_1(-\frac{5}{2})$ are represented on the base of $(|1, -\frac{1}{2}\rangle, |0, \frac{1}{2}\rangle, |-1, \frac{3}{2}\rangle)$, $(|-1, \frac{1}{2}\rangle, |0, -\frac{1}{2}\rangle, |1, -\frac{3}{2}\rangle)$, $(|1, \frac{1}{2}\rangle, |0, \frac{3}{2}\rangle)$, $(|-1, -\frac{1}{2}\rangle, |0, -\frac{3}{2}\rangle)$, $(|1, \frac{3}{2}\rangle)$ and $(|-1, -\frac{3}{2}\rangle)$, respectively. By diagonalizing these submatrices, eigenvalues $E_{J_z, a}$ and eigenvectors $U_{J_z, a}$ are obtained, where $a = 0, \dots, 11$ are the serial numbers for the single-ion states, neither a special quantum number nor the order of energy ($a \neq p$). Three-dimensional vectors $U_{\pm 1/2, a}$ ($a = 0, \dots, 5$) come from $H_1(\pm \frac{1}{2})$, and two-dimensional vectors $U_{\pm 1/2, a}$ ($a = 6, \dots, 9$) arise from $H_1(\pm \frac{3}{2})$. $U_{5/2, 10}$ and $U_{-5/2, 11}$ are equal to 1. The corresponding eigenstates $|J_z, a\rangle$ are written by:

$$\begin{aligned} \left|+\frac{1}{2}, a\right\rangle &= U_{1/2, a} \left(\left|1, -\frac{1}{2}\right\rangle, \left|0, \frac{1}{2}\right\rangle, \left|-1, -\frac{3}{2}\right\rangle\right) \quad \text{for } a = 0, 1, 2, \\ \left|-\frac{1}{2}, a\right\rangle &= U_{-1/2, a} \left(\left|-1, \frac{1}{2}\right\rangle, \left|0, -\frac{1}{2}\right\rangle, \left|1, -\frac{3}{2}\right\rangle\right) \quad \text{for } a = 3, 4, 5, \\ \left|+\frac{3}{2}, a\right\rangle &= U_{3/2, a} \left(\left|1, \frac{1}{2}\right\rangle, \left|0, \frac{3}{2}\right\rangle\right) \quad \text{for } a = 6, 7, \\ \left|-\frac{3}{2}, a\right\rangle &= U_{-3/2, a} \left(\left|-1, -\frac{1}{2}\right\rangle, \left|0, -\frac{3}{2}\right\rangle\right) \quad \text{for } a = 8, 9, \\ \left|+\frac{5}{2}, a\right\rangle &= \left|1, \frac{3}{2}\right\rangle \quad \text{for } a = 10, \\ \left|-\frac{5}{2}, a\right\rangle &= \left|-1, -\frac{3}{2}\right\rangle \quad \text{for } a = 11. \end{aligned} \quad (\text{A} \cdot 5)$$

$$\begin{aligned} H_1 &= c'_{\parallel} \sum_{\mu m} l_{z\mu m}^2 + \lambda' \sum_{\mu m} \mathbf{l}_{\mu m} \cdot \mathbf{S}_{\mu m} \\ &\quad + \sum_{\mu m} \left(2 \sum_r Z_r J_r \langle S_z^{(r)} \rangle \right) S_{z\mu m}, \end{aligned} \quad (\text{A} \cdot 2)$$

$$\begin{aligned} H_2 &= \sum_{\mu m} \sum_{\nu n} J_{\mu m \nu n} \mathbf{S}_{\mu m} \cdot \mathbf{S}_{\nu n} \\ &\quad - \sum_{\mu m} \left(2 \sum_r Z_r J_r \langle S_z^{(r)} \rangle \right) S_{z\mu m}, \end{aligned} \quad (\text{A} \cdot 3)$$

where Z_r is the number of the r th neighbor Co^{2+} ions, $\langle S_z^{(r)} \rangle$ indicates the mean value of $\langle 0 | S_z | 0 \rangle$ among the r th neighbor magnetic ions and $|0\rangle$ is the single-ion ground state.

H_1 is expanded to a 12×12 matrix in the subspace of the twelve $|l_z, S_z\rangle$ base-states representing the Γ_4 states shown in Fig. 1(b). Since eq. (A·2) keeps the value of $J_z = l_z + S_z$ constant, J_z is a good quantum number. Therefore, the 12×12 matrix is resolved to the submatrices $H_1(J_z)$ of $J_z = \pm \frac{1}{2}$, $\pm \frac{3}{2}$, and $\pm \frac{5}{2}$ as described below:

The numerical calculations of H_1 are iterated until convergence of $\langle 0|S_z|0\rangle$ in a successive approximation, where $|0\rangle$ is the single-ion state with a lowest energy. After the convergence, these states are renamed as $|0\rangle$ (the ground state) and $|p\rangle = |1\rangle, \dots, |11\rangle$ in accord with the ascending order of the energy, and the energy is defined as $\varepsilon_p = E_p - E_0$. In this way, we obtain

$$H = \sum_{\mu m} \sum_p \varepsilon_p \hat{a}_{\mu m}^\dagger(p) \hat{a}_{\mu m}(p), \quad (\text{A}\cdot 6)$$

where $\hat{a}_{\mu m}^\dagger(p)$ and $\hat{a}_{\mu m}(p)$ are raising and lowering operators between the $|0\rangle$ and the $|p\rangle$ s, respectively. Table I gives the values of ε_p , the $|0\rangle$ and the $|p\rangle$ s calculated in such way.

The pair interaction H_2 is also described in the form of $\hat{a}_{\mu m}^\dagger(p)$ and $\hat{a}_{\mu m}(p)$ by the following substitution:

$$\begin{aligned} S_{\pm\mu m} &\rightarrow \sum_p \left\{ \langle p|S_{\pm\mu}|0\rangle \hat{a}_{\mu m}^\dagger(p) + \langle 0|S_{\pm\mu}|p\rangle \hat{a}_{\mu m}(p) \right\}, \\ S_{z\mu m} &\rightarrow \langle 0|S_{z\mu}|0\rangle + \sum_p \langle p|S_{z\mu}|0\rangle \left\{ \hat{a}_{\mu m}^\dagger(p) + \hat{a}_{\mu m}(p) \right\} \\ &\quad + \sum_p \left(\langle p|S_{z\mu}|p\rangle - \langle 0|S_{z\mu}|0\rangle \right) \hat{a}_{\mu m}^\dagger(p) \hat{a}_{\mu m}(p), \end{aligned}$$

where $S_{\pm\mu} = S_{\pm\mu m}$ because the sublattices are taken so that magnetic ions in the sublattice are the same.

In the Fourier representation of

$$\begin{aligned} \hat{a}_{\mu q}(p) &= \frac{1}{\sqrt{N_\mu}} \sum_m \hat{a}_{\mu m} \exp(i\mathbf{q} \cdot \mathbf{r}_{\mu m}), \\ \hat{a}_{\mu q}^\dagger(p) &= \frac{1}{\sqrt{N_\mu}} \sum_m \hat{a}_{\mu m}^\dagger \exp(-i\mathbf{q} \cdot \mathbf{r}_{\mu m}), \end{aligned}$$

the total Hamiltonian $H = H_1 + H_2$ is

$$H = \frac{1}{2} (\hat{\mathbf{a}}^\dagger(\mathbf{q}), -\hat{\mathbf{a}}(-\mathbf{q})) \begin{pmatrix} \mathbf{A}(\mathbf{q}) & \mathbf{B}(\mathbf{q}) \\ -\mathbf{B}(-\mathbf{q}) & -\mathbf{A}(-\mathbf{q}) \end{pmatrix} \begin{pmatrix} \hat{\mathbf{a}}(\mathbf{q}) \\ \hat{\mathbf{a}}^\dagger(-\mathbf{q}) \end{pmatrix}, \quad (\text{A}\cdot 7)$$

$$\hat{\mathbf{a}}(\mathbf{q}) = (\hat{a}_{\uparrow q}(1), \dots, \hat{a}_{\uparrow q}(11), \hat{a}_{\downarrow q}(1), \dots, \hat{a}_{\downarrow q}(11)),$$

$$\hat{\mathbf{a}}^\dagger(\mathbf{q}) = (\hat{a}_{\uparrow q}^\dagger(1), \dots, \hat{a}_{\uparrow q}^\dagger(11), \hat{a}_{\downarrow q}^\dagger(1), \dots, \hat{a}_{\downarrow q}^\dagger(11)),$$

$$\mathbf{A}_q = \mathbf{\Delta} + 2\mathbf{h}_{zzq} + \mathbf{h}_{+-q} + \mathbf{h}_{-+q},$$

$$\mathbf{B}_q = 2\mathbf{h}_{zzq} + \mathbf{h}_{++q} + \mathbf{h}_{--q},$$

where the $(\mu p, \mu' p')$ elements of the 22×22 matrices $\mathbf{\Delta}$ and $\mathbf{h}_{\alpha\beta q}$ ($\alpha, \beta = +, -, z$) are

$$\Delta(\mu p, \mu' p') = \varepsilon_p \delta_{\mu\mu'} \delta_{pp'},$$

$$h_{\alpha\beta q}(\mu p, \mu' p') = J_q(\mu, \mu') \langle p|S_{\alpha\mu}|0\rangle \langle 0|S_{\beta\mu'}|p'\rangle.$$

Here,

$$J_q(\mu, \mu') = \sum_{m, m'} J_r \exp\{i\mathbf{q} \cdot (\mathbf{r}_{\mu m} - \mathbf{r}_{\mu' m'})\}$$

Finally, by using the Bogoliubov transformation, we arrive at

$$H = \sum_q \sum_p E_q(p) \hat{\alpha}_q^\dagger(p) \cdot \hat{\alpha}_q(p) \quad (\text{A}\cdot 8)$$

and

$$|(\mathbf{A}_q - \mathbf{B}_q)(\mathbf{A}_q + \mathbf{B}_q) - E_q^2(p)\mathbf{1}| = 0, \quad (\text{A}\cdot 9)$$

$$|(\mathbf{A}_q + \mathbf{B}_q)(\mathbf{A}_q - \mathbf{B}_q) - E_q^2(p)\mathbf{1}| = 0, \quad (\text{A}\cdot 10)$$

where only one determinant of two equations are needed because the eigenvalues are simultaneous solutions of both determinants. It should be also noted that almost all of 22 solutions [= 11 single-ion states \times 2 magnetic moments (\uparrow and \downarrow)] are doubly degenerated like usual magnons in collinear antiferromagnets.

In summary, firstly, we determined the single-ion states $|0\rangle$ and $|p\rangle$ s by using H_1 , secondly, numerically calculated the 22×22 matrices \mathbf{A}_q and \mathbf{B}_q for each \mathbf{q} , and thirdly, obtained a set of $E_q(p)$ by solving the above determinant for each \mathbf{q} .

The following parameters result from the fact that the Co^{2+} ions form the pseudo face-centered cubic unit cell in CoO. The values of Z_r are $Z_1 = 12$, $Z_2 = 6$ and $Z_3 = 24$. The values of $\langle S_z^{(r)} \rangle$ are $\langle S_z^{(1)} \rangle = 0$, $\langle S_z^{(2)} \rangle = \langle 0|S_z|0\rangle$ and $\langle S_z^{(3)} \rangle = 0$, because the first and third neighbor Co^{2+} ions consist of the same numbers of up and down magnetic moments. The relative coordinates, $\mathbf{r}_{\mu m} - \mathbf{r}_{\nu n}$ are represented by $(\frac{1}{2}, \frac{1}{2}, 0)$, $(-\frac{1}{2}, \frac{1}{2}, 0)$, $(\frac{1}{2}, -\frac{1}{2}, 0)$, $(-\frac{1}{2}, -\frac{1}{2}, 0)$ and the eight cyclic coordinates of them for $r = 1$, $(1, 0, 0)$, $(-1, 0, 0)$ and the four cyclic coordinates of them for $r = 2$ and $(\frac{1}{2}, \frac{1}{2}, 1)$, $(-\frac{1}{2}, \frac{1}{2}, 1)$, $(\frac{1}{2}, -\frac{1}{2}, 1)$, $(-\frac{1}{2}, -\frac{1}{2}, 1)$, $(\frac{1}{2}, \frac{1}{2}, -1)$, $(-\frac{1}{2}, \frac{1}{2}, -1)$, $(\frac{1}{2}, -\frac{1}{2}, -1)$, $(-\frac{1}{2}, -\frac{1}{2}, -1)$ and the sixteen cyclic coordinates of them for $r = 3$ in units of the lattice constant, $a \simeq 4.25 \text{ \AA}$.

- 1) J. Kanamori: Prog. Theor. Phys. **17** (1957) 177; J. Kanamori: Prog. Theor. Phys. **17** (1957) 197.
- 2) K. Motizuki: private communications at Kansai University, Spring Meet. Physical Society of Japan, 2000.
- 3) J. Sakurai, W. J. Buyers, R. A. Cowley and G. Dolling: Phys. Rev. **167** (1968) 510.
- 4) T. M. Holden, W. J. L. Buyers, E. C. Svensson, R. A. Cowley, M. T. Hutchings, D. Hukin and R. W. H. Stevenson: J. Phys. C **4** (1971) 2127.
- 5) W. J. L. Buyers, T. M. Holden, E. C. Svensson, R. A. Cowley and M. T. Hutchings: J. Phys. C **4** (1971) 2139.
- 6) R. A. Cowley, P. Martel and R. W. H. Stevenson: Phys. Rev. Lett. **18** (1967) 162.
- 7) P. Martel, R. A. Cowley and R. W. H. Stevenson: Can. J. Phys. **46** (1968) 1355.
- 8) T. Nagamiya: *Jisei no Riron* (Yoshioka Syoten, 1987) Sect. 6, p. 30 [in Japanese].
- 9) S. Itoh, M. Arai and M. Kawai: Appl. Phys. A **74** (2002) Suppl., s198.
- 10) R. E. Watson and A. J. Freeman: Phys. Rev. **120** (1960) 1134.
- 11) M. D. Rechin and B. L. Averbach: Phys. Rev. Lett. **26** (1971) 1483.
- 12) W. Jauch, M. Reehuis, H. J. Blief and F. Kubanek: Phys. Rev. B **64** (2001) 052102.
- 13) K. Tomiyasu, T. Inami and N. Ikeda: Phys. Rev. B **70** (2004) 184411.
- 14) M. Kohgi, Y. Ishikawa and Y. Endoh: Solid State Commun. **11** (1972) 391.
- 15) G. Pepy: J. Phys. Chem. Solids **35** (1974) 433.
- 16) G. E. Kugel, B. Hennion and C. Carabatos: Phys. Rev. B **18** (1978) 1317.
- 17) M. T. Hutchings and E. J. Samuelsen: Phys. Rev. B **6** (1972) 3447.
- 18) A. Abragam and M. H. L. Pryce: Proc. R. Soc. London, Ser. A **205** (1951) 135.
- 19) A. Okazaki and Y. Suemune: J. Phys. Soc. Jpn. **16** (1961) 671.
- 20) W. Jauch, M. Reehuis and A. J. Schultz: Acta Crystallogr., Sect. A **60** (2004) 51.
- 21) B. Morosin: Phys. Rev. B **1** (1970) 236.
- 22) B. T. M. Willis and H. P. Rooksby: Acta Crystallogr. **6** (1953) 827.
- 23) L. C. Bartel and B. Morosin: Phys. Rev. B **3** (1971) 1039.
- 24) R. J. Radwanski and Z. Ropka: Physica B **345** (2004) 107.